



Specific features of the gas-dynamic structure of supersonic axisymmetric microjets of a nonequilibrium SF₆ gas

Vladimir Aniskin, Nikolay Maslov , Sergey Mironov *,
Elena Tsybul'skaya, and Ivan Tsyryulnikov

*Khristianovich Institute of Theoretical and Applied Mechanics,
Siberian Branch of Russian Academy of Sciences, Novosibirsk 630090, Russia*



(Received 6 November 2019; accepted 9 April 2020; published 26 August 2020)

The article explores a physical phenomenon characteristic of the gas dynamics of microflows. Exhaustion of a supersonic jet of a vibrational excited polyatomic gas SF₆ from convergent nozzles with diameters ranging from 63 to 1000 μm is considered. The influence of vibrational nonequilibrium of the gas on the gas-dynamic structure of supersonic axisymmetric jets is detected in experiments and is numerically confirmed. This influence is manifested as a decrease in the streamwise size of the wave structure cells and reduction of the number of these cells as compared to the equilibrium supersonic flow. It is demonstrated that the maximum effect is observed in jets escaping from nozzles with diameters about 250 μm.

DOI: [10.1103/PhysRevFluids.5.083401](https://doi.org/10.1103/PhysRevFluids.5.083401)

I. INTRODUCTION

Under certain conditions, exhaustion of polyatomic gas microjets from nozzles gives rise to physical effects associated with internal degrees of freedom of molecules, which lead to changes in the gas-dynamic structure of microjets, loss of stability of the jet flow, and reduction of the length of the supersonic region. These effects are induced by the fact that the characteristic spatial scale of vibrational relaxation in supersonic microflows of some vibrationally excited gases becomes comparable with the jet flow scale already at atmospheric ambient pressure in the space around the jet. In particular, at atmospheric pressure, the characteristic time of vibrational-translational (v-t) relaxation τ_{vt} of gaseous sulfur hexafluoride (SF₆) is very short (approximately 0.85 μs) [1]; for this reason, the influence of molecule nonequilibrium can be ignored at macroscales, but should be taken into account in high-velocity microflows with the characteristic spatial scale $\sim u\tau_{vt}l_0 \sim v\tau$, where u is the flow velocity. On the other hand, already at room temperature or minor heating, SF₆ molecules ensure large contributions of excited vibrational degrees of freedom to the internal energy. Because of the combination of the short characteristic time of vibrational relaxation of SF₆ molecules and a significant amount of available vibrational energy, the gas-dynamic structure of microflows can be essentially different from that of macroflows.

It is known that the parameters characterizing the jet flow in the case of high-velocity jet exhaustion from sonic nozzles to a submerged space include the jet pressure ratio n , which is the ratio of the static pressure at the nozzle exit to the ambient pressure; this parameter defines the shock wave structure in the jet flow. Moreover, nonisobaric supersonic jets have a specific flow pattern consisting of a sequence of wave cells (barrels) formed due to reflections of shock waves from the jet axis and jet boundary. The values of the gas-dynamic parameters of the jet flow along the streamlines experience periodic changes within the characteristic time t^* as they pass through

*Corresponding author: mironov@itam.nsc.ru

the sequence of wave cells owing to changes in the flow parameters along each cell. This time depends on the jet pressure ratio n and gas flow velocity in the jet; moreover, it is a linear function of the nozzle diameter d . The gas-dynamic structure of the vibrationally excited gas flow can be expected to depend on the ratio t^*/τ and, correspondingly, on the nozzle size. If the time t^* is significantly greater than the relaxation time τ_{vt} and the equilibrium state between the internal and external degrees of freedom of molecules is fast enough to follow the changes in the gas-dynamic parameters along the streamlines, the jet flow can be considered as equilibrium. If $t^* \ll \tau_{vt} t^* \ll \tau$, which may be the case for microjets, then there is not enough time for the equilibrium state to be established, and the gas behaves as a gas without internal degrees of freedom. As there are static pressure variations along the wave structure cells in off-design (overexpanded or underexpanded) jets, it can be expected that the influence of vibrational relaxation on the gas-dynamic structure of the jet is similar to the effect of energy relaxation during propagation of ultrasonic waves in a polyatomic gas. Thus, ultrasonic wave propagation involves sound dispersion in terms of frequency and acoustic wave energy loss due to the so-called molecular absorption [2]. Nevertheless, academic publications provide no experimental data on the influence of vibrational nonequilibrium on flow parameters and cell sizes of the wave structure of the jet flow. Thus, the present paper describes a pioneering study aimed at demonstrating the influence of the nonequilibrium state of polyatomic gases on the gas-dynamic structure of supersonic axisymmetric microjets. The effect of the diameter of sonic micronozzles on the cell size and intensity of variations of flow parameters on the cells of the wave structure of microjets is considered.

II. EXPERIMENTAL EQUIPMENT AND MEASUREMENT TECHNIQUES

The data on the cell size of the wave structure were obtained on the basis of the Schlieren visualization of microjets. An optical rail with a set of optical elements was mounted on a supported optical plate with an active pneumatic system of vibrational isolation (Standa 1VIS10W work station). A 3 W white-light LED with the characteristic size of the luminescent region equal to 3 mm was used as a light source. A UI-3370CP-M video camera (IDS Imaging, Germany) was placed at a distance of 850 mm from the light source for detecting and recording the Schlieren image. The microscope lens with a focal distance of 27 mm and the Foucault knife were located ahead of the camera. The settling chamber with replaceable micronozzles was placed at a distance of 600 mm from the light source. The SF₆ pressure P_0 in the settling chamber was maintained by an FG-201CV digital flowmeter (Bronkhorst, Holland), which was verified by using a 26PC sensor (Honeywell, USA). The microjet escaping from the nozzle propagated normal to the optical axis connecting the light source and the camera; it was illuminated by a quasiparallel light beam. Such a procedure of microjet flow field visualization made it possible to minimize the aberration and interference effects.

The settling chamber could be accurately moved in three directions with respect to the optical axis. The jet exhaustion direction was controlled by using rotating platforms. Using the template located in the focusing plane, the imaging system resolution was measured: 1870 pixels/mm. The template was a needle with calibrated marks. The needle was also used for determining the frontal edge of the nozzle, where significant diffraction was observed. The needle edge located in the focusing plane of the optical system was pressed to the nozzle edge, and its position was established by comparing the resultant image with the needle image.

The video camera data were processed in the following way. Raw images were recorded by our own coded software using an application programming interface provided by the manufacturer. This ensures that no post-processing took place and that the measured signal is proportional to the brightness for each pixel. The image brightness obtained in the case without the jet was subtracted pixel by pixel from the image brightness obtained in the case with the jet. Based on the brightness difference, a new image was constructed with the gray background corresponding to the zero difference. Then this image was normalized to reach the optimal contrast. This procedure allowed

additional minimization of the influence of spurious inhomogeneities in the image field, such as speckles and interference fringes, and improved the image quality.

To compare the numerical simulation results with experimental data the distributions of image brightness along the jet axis x were built. The brightness values in processed images were averaged using ten adjacent to axis pixels. The brightness values were normalized to perform correction for camera gain and offset: $I_{\text{norm}}(x/D) = \frac{I(x/d) - I_{\text{inf}}}{|I_{\text{min}} - I_{\text{inf}}|}$, where d is nozzle diameter, $I(x/d)$ is the measured axial brightness distribution with background and minimal values I_{inf} and I_{min} , respectively.

III. NUMERICAL SIMULATIONS

Numerical simulations were performed by means of solving two-dimensional steady Navier-Stokes equations with a density-based solver (hereinafter ANSYS Fluent terminology is used), second-order implicit scheme in space with the Roe-FDS method of convective flux splitting, and explicit Runge-Kutta method in time. The thermal conductivity κ of the working gas was given by a formula from the kinetic theory, and the gas viscosity μ was given by approximating the data [3] by a polynomial dependence on temperature. The energy of vibrational degrees of freedom is calculated from the characteristic vibrational temperatures in the approximation of the harmonic oscillator. Six-fluoride sulfur has 15 vibrational modes, which are characterized by six vibrational temperatures $\theta_i = \{1114, 926, 1364, 885, 753, 499\}$. For SF₆, two modeling cases—equilibrium and nonequilibrium—were considered. In the case of equilibrium flow, the specific heat at constant pressure c_p was determined as a function of the gas translational-rotational temperature T_{tr} and the characteristic vibrational temperatures θ_i with factors $r_i = \{1, 2, 3, 3, 3, 3\}$ corresponding to the degeneration of modes:

$$\frac{c_p}{R} = 4 + \sum_{i=1}^6 r_i \frac{(\theta_i/T_{\text{tr}})^2 \exp(\theta_i/T_{\text{tr}})}{[\exp(\theta_i/T_{\text{tr}}) - 1]^2}, \quad (1)$$

where R is the specific gas constant. The proposed description of the heat capacity dependence satisfactorily coincides with the data [4,5] in the temperature range 250–350 K with a deviation of less than 1.3%.

To simulate the nonequilibrium of vibrational degrees of freedom of SF₆ molecules, a two-temperature model of relaxation flows was used, in which the energy change of each vibrational mode from time to time was given by the Landau-Teller equation:

$$\frac{de_{v,i}}{dt} = \frac{1}{\tau_{vt}} (e_{v,i}^{\text{eq}} - e_{v,i}). \quad (2)$$

Here $e_{v,i}$ is the vibrational energy of the mode i , $e_{v,i}^{\text{eq}}$ is the local value of the equilibrium vibrational energy of the mode i . The vibrational relaxation time τ_{vt} was assumed to be the same for all vibrational modes. The equilibrium energy of vibrational degrees of freedom was found from the expression

$$e_{v,i}^{\text{eq}} = \frac{\theta_i}{e^{\theta_i/T_{\text{tr}}} - 1} R. \quad (3)$$

With the help of UDS (user defined scalar) and UDF (user defined function)—embedded in the calculation code of user modules, the conservation of vibrational energy of SF₆ molecules equations were added to the Navier-Stokes equations. The energy exchange between vibrational and translational-rotational degrees of freedom with finite relaxation time was also taken into account using UDF, for which the source term $q_{vt,i}$ calculated from the Landau-Teller equation was added to the embedded equations for the conservation of vibrational energy of each vibrational mode. To exclude energy balance disturbances in the system of Navier-Stokes equations, the same expressions were added to the relations for translational-rotational energy, but with the opposite sign. The system

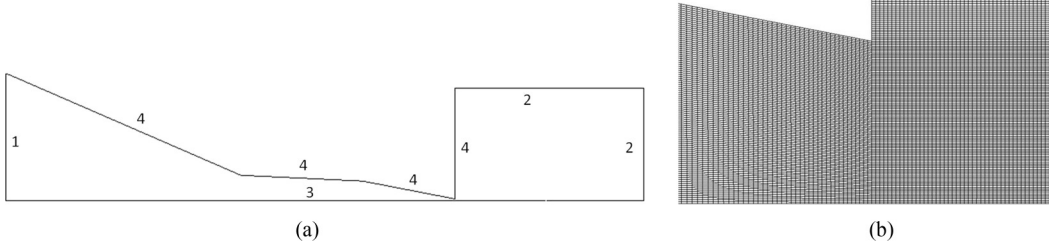


FIG. 1. Contour of the computational domain (a) and computational grid near the nozzle throat (b). 1 inlet boundary, 2 outlet boundary, 3 axis of symmetry, and 4 wall.

of equations in this case takes the following form:

$$\begin{aligned}
 \frac{\partial \rho}{\partial t} + \nabla(\rho \mathbf{u}) &= 0, \\
 \frac{\partial}{\partial t}(\rho \mathbf{u}) + \nabla(\rho \mathbf{u} \mathbf{u}) &= -\nabla P + \nabla \tau_{\mu}, \\
 \frac{\partial}{\partial t}(\rho E_{tr}) + \nabla[\mathbf{u}(\rho E_{tr} + P)] &= \nabla(\kappa \nabla T_{tr} + \tau_{\mu} \mathbf{u}) - \sum_{i=1}^6 r_i q_{vt,i}, \\
 \frac{\partial}{\partial t}(\rho e_{v,i}) + \nabla(\mathbf{u} \rho e_{v,i} - \mu \nabla e_{v,i}) &= q_{vt,i}.
 \end{aligned} \tag{4}$$

Here ρ , P is density and pressure, \mathbf{u} is the velocity vector, τ_{μ} is the tensor of viscous stresses, $E_{tr} = \int_{T_{ref}}^{T_{tr}} c_{p,0} dT_{tr} - \frac{P}{\rho} + \frac{\mathbf{u}^2}{2}$ is the translational and rotational energy of gas, $q_{vt,i} = \frac{\rho}{\tau_{vt}} (e_{v,i}^{eq} - e_{v,i})$, $c_{p,0}$ is the specific heat at constant pressure, associated with translational and rotational degrees of freedom, and T_{ref} is the reference temperature for the enthalpy calculation. The vibrational relaxation time of SF₆ molecules was calculated by approximating the data [1] by a dependence that has the form

$$P \tau_{vt} = \exp(38.0 T_{tr}^{-1/3} - 8.126) [\text{Pa s}].$$

The computational domain shown in Fig. 1(a) was chosen for modeling axisymmetric microjets with due allowance for the flow in a real duct of a sonic nozzle. The computational domain contained a subdomain containing the nozzle duct and the settling chamber, which was finalized by the nozzle throat with a radius $d/2$, as well as the jet exhaustion region (external space with respect to the jet) with the size of $50d$ along the axis and $30d$ over the radius. The domain was covered by a rectangular grid, which was refined toward the jet axis along the radius and toward the nozzle throat along the jet axis [Fig. 3(b)]. The values of the total pressure and temperature (P_0 , T_0) were imposed on the left boundary of the computational domain (settling chamber); exhaustion of the same gas with $P_{inf} = 0.1$ MPa and $T_{inf} = 300$ K into the atmosphere was implied on the external boundaries of the external space with respect to the jet; finally, the condition of symmetry was imposed on the lower boundary (nozzle axis). The nozzle walls were subjected to the no-slip condition and the equality of vibrational temperature, translational-rotational temperature, and wall temperature $T_v = T_{tr} = T_w = 300$ K.

Numerical simulations of nonequilibrium SF₆ jets were performed only for one value of the total pressure $P_0 = 0.2324$ MPa and total temperature $T_0 = 300$ K, which corresponds to the jet pressure ratio $n = 1.363$. The nozzle diameter d was varied from 18.5 to 1000 μm . In all test cases, the Reynolds number of jet exhaustion Re_d was significantly greater than 2000. It was demonstrated in earlier experiments that axisymmetric microjets of air at such values of Re_d are always turbulent [6]. Therefore, the $k-\omega$ SST turbulence model was used.

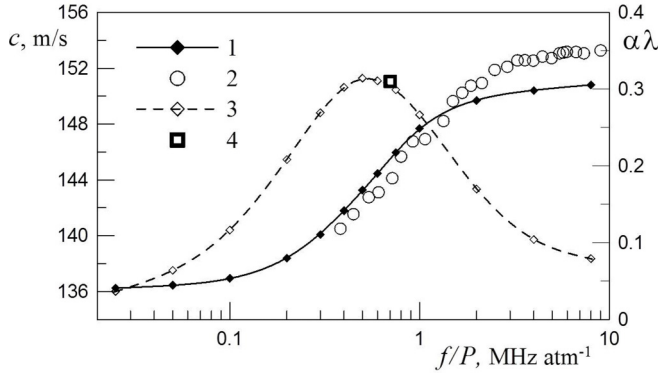


FIG. 2. Frequency dispersion of the speed of sound. (1) the speed of sound calculated for a model gas at $T_{tr} = 300$ K; (2) the speed of sound in the experiment [7] at $T_{tr} = 309.25$ K; (3) sound absorption coefficient per wavelength for a model gas; and (4) maximum sound absorption coefficient according to [8].

IV. RESULTS OF EXPERIMENTS AND NUMERICAL SIMULATIONS OF SF₆ JETS

Before calculating the jet flows, the model problem of the sound propagation in SF₆ at atmospheric pressure was considered. A two-dimensional computational domain of large extent with symmetry type conditions at the lateral boundary was used. A piston was placed on the left boundary of the domain which oscillated according to a harmonic law with a given frequency. The piston excites a sound wave that propagates along the computational domain. From the obtained data the values of the wavelength λ and the sound speed c were determined, as well as the coefficients of sound attenuation α . It turned out that the attenuation is well described by an exponential law. Figure 2 shows the values of the sound speed depending on the frequency. Curve (1): values of the sound speed obtained in numerical simulation at a temperature of $T_{tr} = 300$ K. It can be seen that in the model gas there is an effect of frequency dispersion of the sound speed. At low frequencies, when the vibrational degrees of freedom have time to relax, the speed of sound takes the value c_0 , the so-called equilibrium speed of sound. At high frequencies of sound, when the vibrational degrees are frozen, the speed of sound takes the value c_∞ . For comparison, symbols (2) show the experimental data on the speed of sound in SF₆ at $T_{tr} = 309.25$ K from [7]. Between c_0 and c_∞ there is a region of relatively rapid change in the speed of sound as a function of frequency and a corresponding region of strong sound absorption caused by vibrational relaxation. This effect is phenomenologically described by the occurrence of bulk viscosity. Curve (3) shows the values of the sound absorption coefficient per wavelength $\alpha\lambda$, which takes the highest values corresponding to the acoustic wavelength $\lambda^* = 250 \mu\text{m}$. For comparison, point (4) shows the value of the sound absorption coefficient calculated from the data of [8]. It can be noted that the gas model used in this study is consistent with experimental data on the frequency dispersion and sound attenuation effect.

Figure 3 shows several examples of the Schlieren patterns of supersonic SF₆ microjets for $n = 1.363$ escaping into air from micronozzles with diameters $d = 63, 90, 260, 341,$ and $1000 \mu\text{m}$ [Figs. 3(a)–3(e), respectively]. The Foucault knife is aligned orthogonal to the jet axis. The image scales are different; therefore, they are normalized to a unified value of the image size to the nozzle diameter. It is seen that the all jet flow fields contain wave structure cells corresponding to image brightness variations. However, the number of gas-dynamic cells seen in the images is different, depending on the nozzle diameter. The number of visible cells is four or more for the smallest nozzle with $d = 63 \mu\text{m}$ and for the greatest nozzle with $d = 1000 \mu\text{m}$, but the number of cells that can be seen for nozzles with intermediate diameters is no more than three. Moreover, changes in the normalized sizes L_s/d of the first and next cells are observed. These features of the flow are considered in more detail below. A specific feature of visualization of these jet flows is the

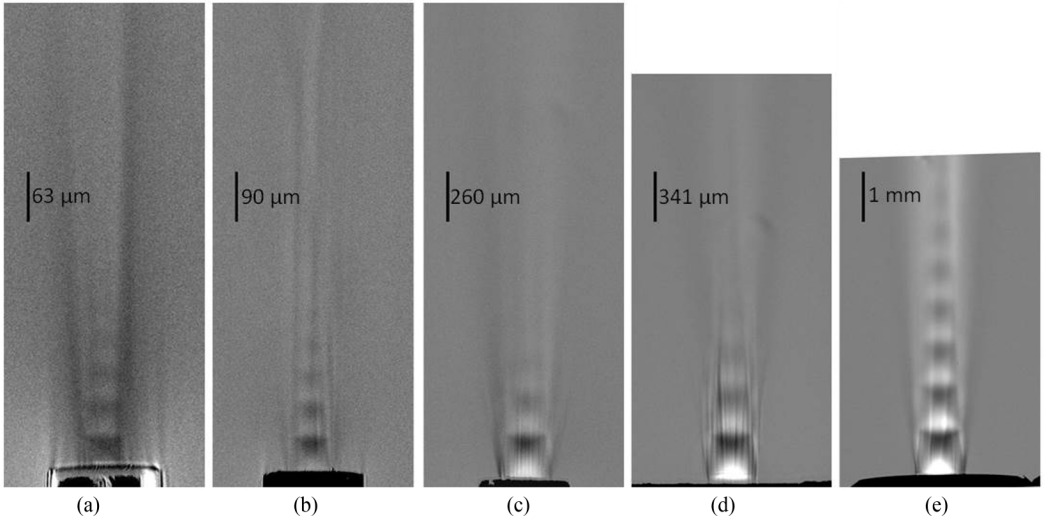


FIG. 3. Schlieren visualization of supersonic SF_6 microjets with $n = 1.363$ escaping into air from micronozzles of different diameters: $d = 63$ (a), 90 (b), 260 (c), 341 (d), and $1000 \mu\text{m}$ (e).

emergence of clearly expressed streamwise structures, especially at $d > 260 \mu\text{m}$, which is most probably associated with the development of the Goertler vortices. However, the issues of flow turbulization and vortex formation in SF_6 jets are not considered here in much detail.

Figure 4 shows the results of the numerical Schlieren visualization of SF_6 microjets with $n = 1.363$ escaping into the submerged space. The scales of the images in Fig. 4 correspond to the scales of the images in Fig. 3. The simulations were performed for nozzle diameters $d = 63, 90, 260, 341,$ and $1000 \mu\text{m}$ [Figs. 4(a)–4(e), respectively], which is consistent with the micronozzle diameters used in the experiments. The nonequilibrium character of the SF_6 flow was taken into account. For comparison, Fig. 4(f) shows the numerical Schlieren pattern for a supersonic jet of the equilibrium SF_6 gas with the same jet pressure ratio exhausting from the nozzle with $d = 260 \mu\text{m}$. The equilibrium computations show that the gas-dynamic structure of microjets remains almost

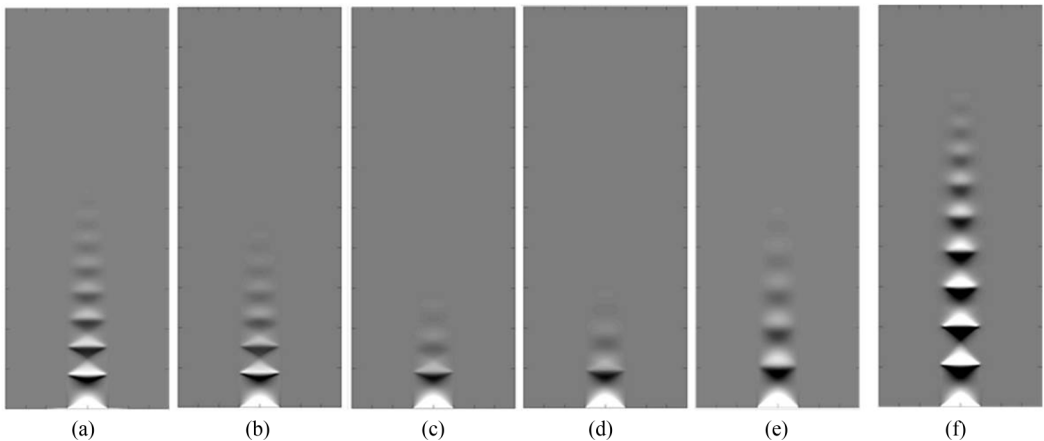


FIG. 4. Numerical Schlieren visualization of supersonic SF_6 microjets with $n = 1.363$ escaping into air from micronozzles of different diameters: $d = 63$ (a), 90 (b), 260 (c), 341 (d), and $1000 \mu\text{m}$ (e); equilibrium flow for $d = 260 \mu\text{m}$ (f).

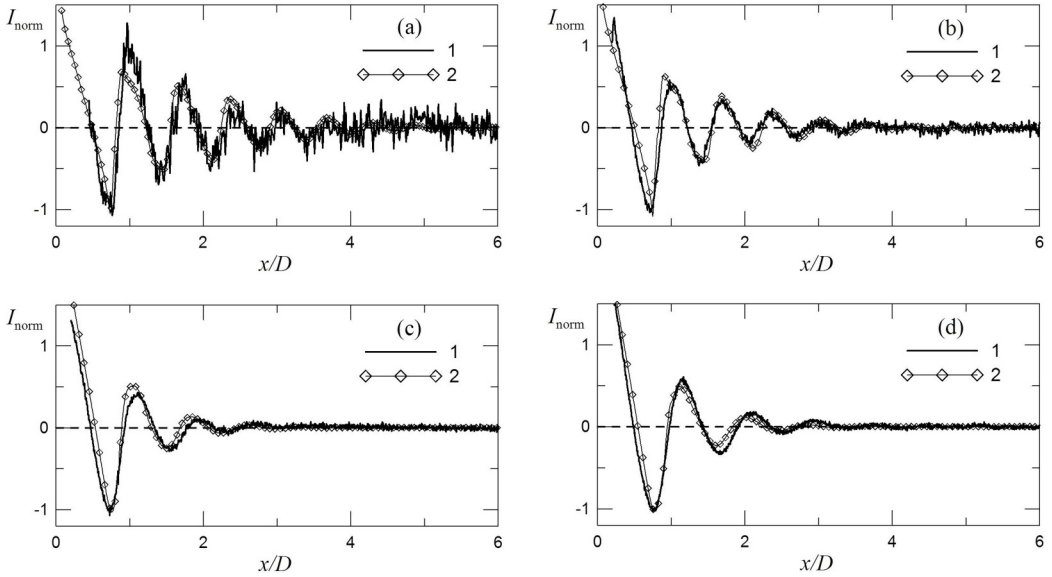


FIG. 5. Axial distributions of normalized brightness of Schlieren images in experiment (1) and numerical simulation (2) for microjets nozzle $d = 63 \mu\text{m}$ (a), $90 \mu\text{m}$ (b), $260 \mu\text{m}$ (c), and $341 \mu\text{m}$ (d).

unchanged in the examined range of nozzle diameters. It is seen in Fig. 4 that the number of cells of the wave structure and the relative size of these cells in the nonequilibrium SF_6 flow in numerical simulations varies within wide limits depending on the nozzle diameter, similar to that observed in experiments (see Fig. 3). It can be also noted that the number of cells of the wave structure in the nonequilibrium flows in Figs. 4(a)–4(e) is smaller than the number of cells in the equilibrium case.

Figure 5 shows examples of comparisons of axial brightness distributions of Schlieren images and calculated data for four nozzle diameters. Curves (1) show normalized experimental values of image brightness. Curves (2) show the calculated values of the longitudinal density gradient integrated in the direction of observation in a normalization similar to the experimental one. It can be seen that the number of cells for jets of smaller diameter is larger and their size is slightly reduced. The relative sizes and the number of cells in the jet stream in numerical modeling, as well as the values of normalized integral density gradients, satisfactorily coincide with the experimental data.

Figure 6 shows the predicted streamwise distributions of the static pressure P along the axis of the jet escaping from the micronozzle with the diameter of $260 \mu\text{m}$ for the nonequilibrium (solid curves) and equilibrium (dotted curves) SF_6 jets. It is seen that the variations of the pressure P decay along the gas-dynamic cells, i.e., the maximum and minimum values of P in a gas-dynamic cell become much smaller than the corresponding values in the previous cell and that the corresponding values for the equilibrium flow.

To illustrate the effect of attenuation of flow parameter variations along the cells of the wave structure of the SF_6 jet, Fig. 7 shows the ratio of the maximum difference of the pressures $\Delta P_{\text{noneq}} = P - P_{\text{inf}}$ along the j th gas-dynamic cell in the nonequilibrium jet to the maximum difference of the pressures ΔP_{eq} along the same cell in the equilibrium jet versus the nozzle diameter d . Points (1)–(4) show the corresponding values of j . It is seen that the effect of vibrational-translational relaxation on the jet structure and damping of variations is observed in a wide range of nozzle diameters. The shape of the curve $(\frac{P_{\text{noneq}} - P_{\text{inf}}}{P_{\text{eq}} - P_{\text{inf}}})_j$ has the minimum value corresponding to the nozzle diameter $d^* = 260 \mu\text{m}$, where the most pronounced effect of nonequilibrium on the jet structure is observed. Attenuation of parameter variations on the cells can be also defined by the damping coefficient, which has a domelike shape with the maximum at d^* . Similar dependences for the damping

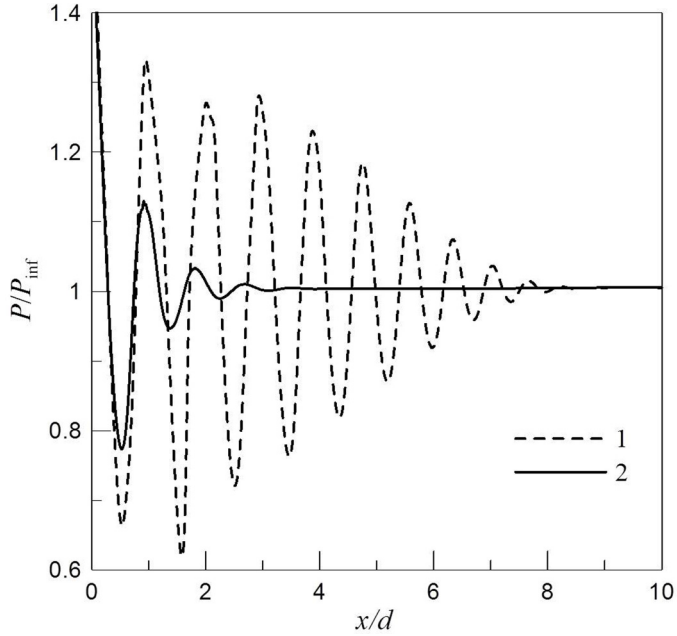


FIG. 6. Calculated static pressure at the SF_6 jet axis for $n = 1.363$ and nozzle diameter $d = 260 \mu\text{m}$; curves 1 and 2 show the results for the equilibrium and nonequilibrium flows, respectively.

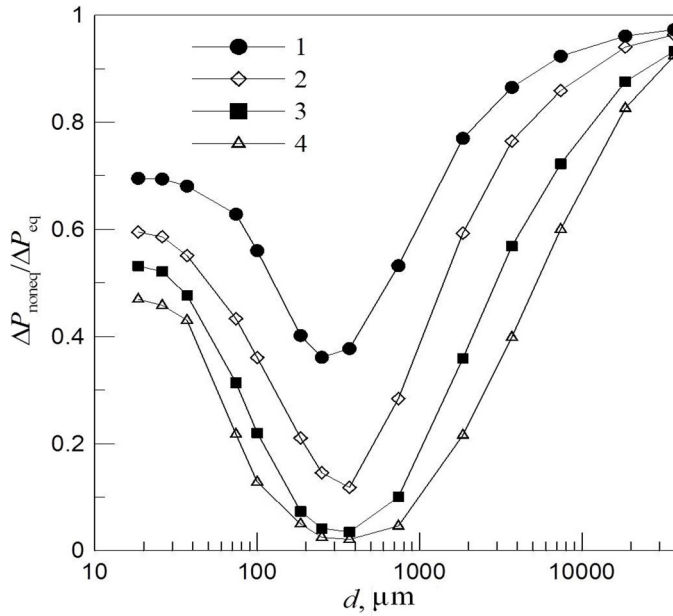


FIG. 7. Ratio of the amplitudes of static pressure variations along the wave structure cells for nonequilibrium and equilibrium SF_6 jets with $n = 1.363$: the data for the first to fourth cells are indicated by the numbers 1 to 4, respectively.

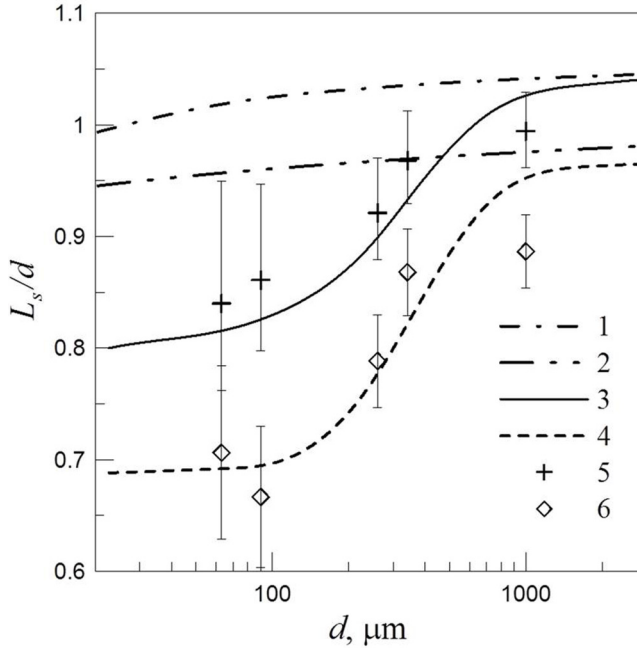


FIG. 8. Length of the cells of the wave structure of the SF₆ jet with $n = 1.363$: calculated streamwise size of the first cell in the equilibrium case (1); calculated mean cell size in the equilibrium case (2); calculated streamwise size of the first cell in the nonequilibrium case (3); calculated mean cell size in the nonequilibrium case (4); streamwise size of the first cell in the experiment (5); and mean cell size in the experiment (6).

coefficients of sound are observed in the presence of energy exchange between translational, vibrational, and rotational motions of molecules in physical acoustics, resulting in dispersion in terms of frequency and energy loss of the acoustic wave. A variable phenomenologically characterizing this process of energy dissipation is the bulk viscosity, which determines the sound absorption coefficient.

In the present study we found that the cell size of the wave structure depends on the nozzle diameter. This dependence is illustrated in Fig. 8. Curves (1) and (2) show the normalized streamwise sizes L_s/d for the first cell of the wave structure and the averaged size for cells 2–4, respectively, which were obtained in modeling equilibrium jets. As the nozzle diameter is varied within wide limits, the size of the first gas-dynamic cell slightly decreases ($\approx 2\%$) with a decrease in the nozzle diameter d , and the mean cell size remains almost constant. At the same time, for the first cell size (curve 3 in Fig. 8) and mean size of the gas-dynamic cell (curve 4 in Fig. 8) in the nonequilibrium case, the values of L_s/d equal to 0.8 and 0.69 for small nozzle diameters change to 1.0 and 0.95 for nozzle diameters of the order of 1 mm, which is fairly close to the values calculated in the equilibrium case. The data for the streamwise size of the first cell of the wave structure and the mean cell size obtained on the basis of flow visualization are shown in Fig. 8 by points (5) and (6), respectively. It is seen that the effect of the nozzle diameter on the gas-dynamic cell size is also detected in the experiment, and the result of numerical simulations agree well with the experimental data on the gas-dynamic cell size.

It should be noted that the maximum change in the cell size due to variations of the nozzle diameter is observed for the nozzle diameter approximately equal to d^* , which ensures the maximum effect of damping of parameters variations on the cells of the wave structure of the jet. In this case, the values of the cell length L_s^* corresponding to d^* obtained in numerical simulation turned out to be close to the value of the sound wavelength λ^* at which the greatest effects associated

with the dispersion of sound speed are observed. At $d < 100 \mu\text{m}$, the characteristic exhaustion time is insufficient for the relaxation processes of vibrational degrees of freedom in the SF_6 jet to be finalized, and they exert practically no effect on the flow. As a result, the effective specific heat of the gas is determined only by translational-rotational degrees of freedom, $c_p \approx c_{p,o} = 4R$, and the effective velocity of sound, which is responsible for the cell size of the wave structure of the jet, corresponds to its high-frequency dispersion limit. Thus, there is an analogy between the dependence of the cell size of the wave structure of the jet on the nozzle diameter and the frequency dispersion in the case of sound propagation in a nonequilibrium gas, where the maximum absorption coefficient due to bulk viscosity coincides with the maximum change in the velocity of sound in terms of frequency.

V. CONCLUSIONS

Calculations are performed for determining the influence of vibrational relaxation of the gas on the gas-dynamic structure of SF_6 jets. The effect of vibrational relaxation is taken into account within the framework of the two-temperature model of relaxation flows with a finite time of energy exchange between translational-rotational and vibrational degrees of freedom. Under the conditions of the present study, the effect of the nozzle diameter on the streamwise size of the cells of the wave structure of the supersonic jet is evaluated; the variations of the flow parameters along the jet axis are found to be smaller than those in the equilibrium jet flow, and the number of cells of the wave structure is also smaller in the nonequilibrium case. These effects can be attributed to the emergence of additional bulk viscosity of the gas in the considered flows, which is induced by thermal relaxation of gas molecules. The influence of the nozzle diameter on the streamwise size of gas-dynamic cells and attenuation of the flow parameter variations along the gas-dynamic cells of a supersonic axisymmetric SF_6 jet are experimentally demonstrated.

ACKNOWLEDGMENT

The research was carried out within the framework of the Program of Fundamental Scientific Research of the State Academies of Sciences in 2013–2020 (Project No. AAAA-A17-117030610126-4).

-
- [1] W. D. Breshears and L. S. Blair, Vibrational relaxation in polyatomic molecules: SF_6 , *J. Chem. Phys.* **59**, 5824 (1973).
 - [2] V. A. Krasilnikov, *Acoustic Waves in Air, Water and Solid Bodies* (Phys.-Math., Moscow, 1960) [in Russian].
 - [3] V. G. Arakelyan, *Physical Chemistry of ELEGAS Electro-Technical Equipment* (Moscow Energetic Institute, Moscow, 2001) [in Russian].
 - [4] E. W. Lemmon, M. O. McLinden, and D. G. Friend, Thermophysical properties of fluid systems, *NIST Chemistry WebBook*, NIST Standard Reference Database Number 69 (Gaithersburg, MD, 2018).
 - [5] W. A. Cole and K. M. de Reuk, An interim analytic equation of state for sulfur fluoride, *Int. J. Thermophys.* **11**, 189 (1990).
 - [6] V. M. Aniskin, S. G. Mironov, A. A. Maslov *et al.*, Supersonic axisymmetric microjets. Structure and laminar–turbulent transition, *Microfluidics Nanofluidics* **19**, 621 (2015).
 - [7] C. L. O’Connor, Thermal relaxation of vibrational states in sulfur hexafluoride, *J. Acoust. Soc. Am.* **26**, 361 (1954).
 - [8] R. Holmes and M. A. Stott, Temperature dependence of vibrational relaxation times in cyclopropane, ethylene and sulphur hexafluoride, *J. Phys. D* **1**, 1331 (1968).